



Controllable synthesis of multi-responsive ferroelectric layered perovskite-like $\text{Bi}_4\text{Ti}_3\text{O}_{12}$: Photocatalysis and piezoelectric-catalysis and mechanism insight



Shuchen Tu^a, Hongwei Huang^{a,*}, Tierui Zhang^b, Yihe Zhang^{a,*}

^a Beijing Key Laboratory of Materials Utilization of Nonmetallic Minerals and Solid Wastes, National Laboratory of Mineral Materials, School of Materials Science and Technology, China University of Geosciences, Beijing 100083, China

^b Key Laboratory of Photochemical Conversion and Optoelectronic Materials, Technical Institute of Physics and Chemistry, Chinese Academy of Sciences, Beijing 100190, China

ARTICLE INFO

Article history:

Received 18 April 2017

Received in revised form 29 June 2017

Accepted 1 August 2017

Available online 2 August 2017

Keywords:

Piezoelectric-catalytic

Photocatalytic

$\text{Bi}_4\text{Ti}_3\text{O}_{12}$

Morphology control

Radicals

ABSTRACT

Development of multi-responsive catalytic materials is a highly meaningful and challenging subject for forwarding the understanding on catalysis mechanism. In this work, we for the first time disclose the piezoelectric-catalytic performance and morphology-dependent photocatalytic activity of $\text{Bi}_4\text{Ti}_3\text{O}_{12}$. Via introducing and manipulating the mineralizer sodium hydroxide, we developed a series of $\text{Bi}_4\text{Ti}_3\text{O}_{12}$ catalysts with diverse morphologies, including nanorods, slice-assembled microspheres, nest-like hollow microspheres, and cube assembly. The photocatalytic activity of these hydrothermally-yielded $\text{Bi}_4\text{Ti}_3\text{O}_{12}$ as well as sol-gel derived $\text{Bi}_4\text{Ti}_3\text{O}_{12}$ is investigated by degradation of phenol, and the photocatalytic mechanism is explored. The $\text{Bi}_4\text{Ti}_3\text{O}_{12}$ microsphere exhibits the most efficient degradation activity, and also presents universal photoreactivity for removing multiform contaminants and antibiotics, like bisphenol A, rhodamine B, chlorotetracycline and tetracycline hydrochloride, boding for its promising practical applications. Significantly, $\text{Bi}_4\text{Ti}_3\text{O}_{12}$ demonstrates a high piezoelectric-catalytic performance for ultrasonic-assisted decomposition of methyl orange, bisphenol A and tetracycline hydrochloride. It is uncovered that both powerful superoxide ($\bullet\text{O}_2^-$) and hydroxyl ($\bullet\text{OH}$) radicals are generated with production rates of 6.4 and $2.4 \mu\text{mol g}^{-1} \text{h}^{-1}$, respectively, which take crucial roles in the piezoelectric-catalytic process. The corresponding mechanism is tentatively speculated. This work may push forward to the development of multi-responsive catalytic materials, and provide insights into piezoelectric-catalysis for environmental applications.

© 2017 Elsevier B.V. All rights reserved.

1. Introduction

Layered bismuth-based materials, such as Sillén-structured BiOX ($\text{X} = \text{Cl}, \text{Br}, \text{I}$) family [1–3], Aurivillius-structured Bi_2WO_6 [4], and Sillén-structure-related $\text{Bi}_2\text{O}_2\text{CO}_3$ [5], $\text{Bi}_2\text{O}_2[\text{BO}_2(\text{OH})]$ [6] and $\text{Bi}_2\text{O}_2(\text{OH})(\text{NO}_3)$ [7] have harvested special interests recently. Crystal structure of these materials are always composed of $\text{Bi}_2\text{O}_2^{2+}$ fluorite-structure layers and interleaved halide ions or perovskite-like $(\text{A}_{m-1}\text{B}_m\text{O}_{3m+1})^{2-}$ or $\text{CO}_3^{2-}/\text{BO}_3^{3-}/\text{NO}_3^-$ anionic blocks. Such orderly layered structure was believed prone to form internal electric field [8] and realize the effective charge separation, which enables these materials to achieve an enhanced photocatalytic activity [9], thus triggering substantial interests of researchers.

Bismuth titanate ($\text{Bi}_4\text{Ti}_3\text{O}_{12}$) is known as a widely-studied leadless piezoelectric ceramic. It is reported that the $\text{Bi}_2\text{O}_2^{2+}$ fluorite-structure attributes a large amount of oxygen vacancies [10], which could extend the wavelength coverage of light response. Another important positive factor for photocatalysis may be the strong spontaneous polarization engendered in the ferroelectric $\text{Bi}_4\text{Ti}_3\text{O}_{12}$ crystal, which can efficiently separate the photoexcited carriers due to the internal space charge layer analogous to BaTiO_3 [11]. As we all know, microstructure of semiconductor is closely associated with its photoactivity. Among the synthetic methods of $\text{Bi}_4\text{Ti}_3\text{O}_{12}$, hydrothermal [12], solvothermal [13] and sol-gel synthesis [14] were demonstrated capable of acquiring a regular spherical structure compared with the frequently used solid-state reaction, through adding suitable mineralizer in hydrothermal process [15,16]. However, tedious morphology (e.g. only one single type of unordered nanosheet) has been achieved in the previously reported work. Thus, development

* Corresponding authors.

E-mail addresses: hhw@cugb.edu.cn (H. Huang), zyh@cugb.edu.cn (Y. Zhang).

of $\text{Bi}_4\text{Ti}_3\text{O}_{12}$ materials with diverse morphologies, and particularly exploration on the morphology-dependent photocatalytic performance is challenging and meaningful.

Multiferroic materials easily undergo bending or deformation and produce electric charges on their surface when subjected to mechanical vibration due to the piezoelectric effect. The same principle can be introduced to induce a catalytic reaction called piezoelectric-catalysis, after the discovery that ultrasonic can replace direct press to bend or deform the nano-sized piezoelectric materials [17,18]. Recently, dendritic BaTiO_3 is found capable of hydrogen production from water splitting with the help of ultrasonic waves, where direct conversion of mechanical energy to chemical energy reveal that active species produced by the piezoelectric material can trigger the redox reaction in water [19]. Further study demonstrated that the induced electric charges can be used to realize degradation of dye in wastewater through the electro-catalytic effect [20], where strongly oxidative h^+ and $\cdot\text{OH}$ are generated in the ultrasonic process and cause the degradation reactions of the dyes in solution [21,22]. So far, very few researches about piezoelectric-catalysis have been reported yet and BaTiO_3 is the only object investigated in this field. In particular, the piezoelectric-catalysis mechanism, like how the piezoelectric effect triggers the catalytic reaction for degradation, still remains vague. Considering the ferroelectricity of $\text{Bi}_4\text{Ti}_3\text{O}_{12}$, it may be a suitable model to investigate both the photocatalytic and piezoelectric-catalytic properties.

In this work, we developed a series of $\text{Bi}_4\text{Ti}_3\text{O}_{12}$ with diverse morphologies via one-pot hydrothermal process, including nanorods, slice-assembled microspheres, nest-like hollow microspheres, and cube assembly by manipulating the mineralizer concentration. The photocatalytic activity of these hydrothermally-prepared $\text{Bi}_4\text{Ti}_3\text{O}_{12}$ as well as the sol-gel-yielded counterpart is investigated by degradation of phenol, and universal photoreactivity is also explored through removing multiform contaminants and antibiotics, like bisphenol A, rhodamine B, chlorotetracycline and tetracycline hydrochlorid. Additionally and importantly, we for the first time unearth that $\text{Bi}_4\text{Ti}_3\text{O}_{12}$ shows an ultrasonic-assisted piezoelectric-catalytic performance for degradation of methyl orange. It produces abundant powerful superoxide ($\cdot\text{O}_2^-$) and hydroxyl ($\cdot\text{OH}$) radicals in the piezoelectric-catalytic process, accounting for the efficient degradation. The corresponding catalytic mechanism is also proposed. Our study set a good instance for developing multi-responsive catalytic materials for environmental applications.

2. Experimental section

2.1. Sample preparation

All chemicals used in this work were analytical reagent grade without further purification process. $\text{Bi}_4\text{Ti}_3\text{O}_{12}$ was synthesized by a hydrothermal method. In a typical operation, 0.84 g tetra-butyl titanate was added and dispersed into 30 mL prepared sodium hydroxide solution with NaOH concentrations of 1, 3, 5, 7, 10 and 15 M at room temperature. Then, certain amount of bismuth nitrate pentahydrate was added to the above solution with the Bi:Ti molar ratio of 4:3, and the mixed solution was continuously magnetic-stirred for 0.5 h and ultrasonic-dispersed before transferred into a 50 mL Teflon-lined stainless autoclave and heated at 180 °C for 20 h. After cooling, the products were filtered, washed with deionized water and absolute ethyl alcohol for each 3 Times, the obtained samples were collected and dried at 80 °C in air for 6 h.

$\text{Bi}_4\text{Ti}_3\text{O}_{12}$ were also prepared via conventional sol-gel synthesis with subsequent solid-phase calcination processing (SG- $\text{Bi}_4\text{Ti}_3\text{O}_{12}$ for short) with the reported procedure [23].

2.2. Characterization

Bruker D8 focus with Cu K α radiation was employed to analyze the crystalline structure of the obtained samples. The morphology and microstructure of the products were investigated by S-4800 scanning electron microscope (SEM), and energy dispersive spectroscopy (EDS) attached to the SEM was used to examine the composition of the products at the same time. Transmission electron microscopy (TEM) and high-resolution transmission electron microscopy (HRTEM) images were obtained using a JEM-2100 electron microscopy (JEOL, Japan). Specific surface areas of the samples were characterized by the nitrogen adsorption BET method with a Micromeritics 3020 instrument. UV-vis diffuse reflectance spectra (DRS) were recorded from a PerkinElmer Lambda 35 UV-vis spectrometer. The spectra were collected at 200–800 nm, referenced to BaSO_4 . Photoluminescence (PL) spectra of the as-prepared samples were measured using a Hitachi F-4600 fluorescence spectrophotometer (Tokyo, Japan) to determine the recombination rate of electron–hole pairs.

2.3. Photocatalytic evaluation

The photocatalytic activity of $\text{Bi}_4\text{Ti}_3\text{O}_{12}$ series was evaluated by photodegradation of the phenol under ultraviolet light with a 300 W high-temperature mercury lamp. 0.05 g of as-prepared $\text{Bi}_4\text{Ti}_3\text{O}_{12}$ was dispersed into 50 mL of 20 mg/L phenol solution. The mixture was firstly stirred in the dark for 40 min to ensure a complete adsorption–desorption equilibrium of the phenol by the catalyst, and then exposed to ultraviolet light with the mercury lamp on, about 3 mL of the suspension was taken at certain intervals during irradiation. All the suspension samples were separated through centrifugation before determined. The concentration of phenol was determined by recording the absorption spectra of the residual phenol by a Cary 5000 UV-vis spectrophotometer based on the absorbance at 270 nm.

The photocatalytic performance of $\text{Bi}_4\text{Ti}_3\text{O}_{12}$ was also investigated by degradation of various pollutants including rhodamine B (1×10^{-5} M), bisphenol A (10 mg/L), chlorotetracycline (20 mg/L), tetracycline hydrochloride (10 mg/L). A total of 20 mg of photocatalyst was dispersed in 40 mL of pollutant aqueous solution and the suspension was exposed to UV-vis light provided by a 500 W xenon lamp. The rest procedure was followed as described above.

2.4. Active species trapping experiment for photocatalysis

For revealing the active species participating in the photocatalytic degradation process, disodium ethylenediaminetetraacetate (EDTA-2Na) and isopropyl alcohol (IPA) were chosen as the hole (h^+) scavenger and hydroxyl radical ($\cdot\text{OH}$) scavenger [24], respectively. In view of that *p*-benzoquinone (the frequently-used scavenger for superoxide radical ($\cdot\text{O}_2^-$)) is unstable in phenol solution, high-purity argon was bubbled into sealed quartz tube to eliminate O_2 to inspect the formation of superoxide radical ($\cdot\text{O}_2^-$), and the following processes were similar to the above photodegradation experiment. The concentration of phenol was determined by recording the absorption spectra of the residual phenol by a Cary 5000 UV-vis spectrophotometer based on the absorbance at 270 nm.

2.5. Ultrasonic-assisted piezoelectric-catalytic degradation

200 mg of $\text{Bi}_4\text{Ti}_3\text{O}_{12}$ sample and 150 mL of methyl orange solution (1×10^{-5} M) were added into 250 mL boiling flask-3-neck located inside an ultrasonic cleaner (40 kHz, power adjustable, max: 300 W) equipped with an electric stirrer. The temperature of this system was maintained below 45 °C all the time with frequent water inflow-outflow operation. Photomask was covered

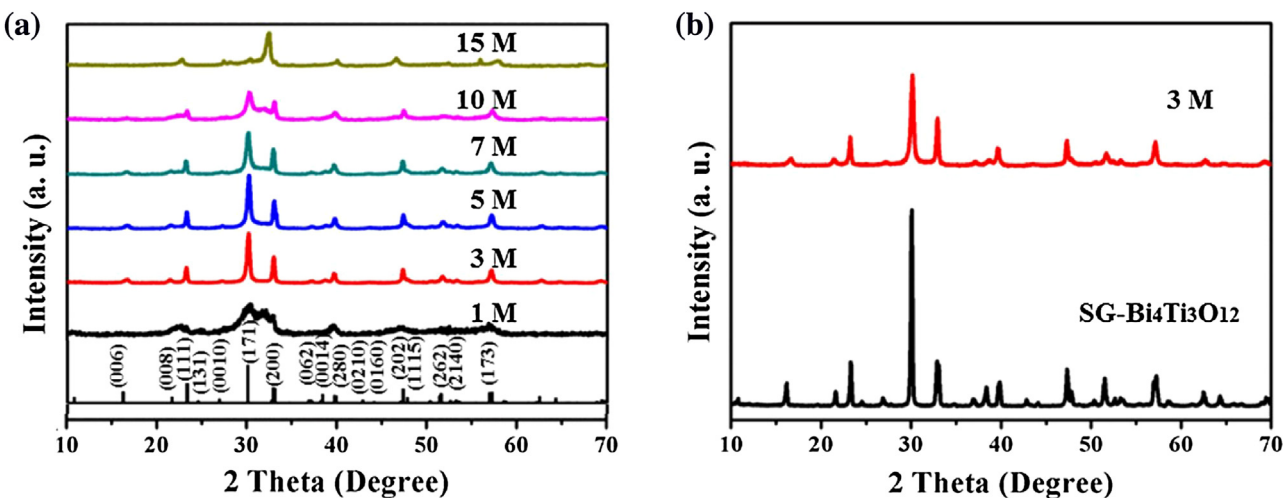


Fig. 1. XRD patterns: (a) Hydrothermally-synthesized samples with different NaOH concentration; (b) Comparison of hydrothermal Bi₄Ti₃O₁₂ (3 M NaOH) and SG-Bi₄Ti₃O₁₂ synthesized by sol-gel method.

the top of the ultrasonic cleaner to kept away from any light. The ultrasonic-assisted piezoelectric-catalytic degradation experiment is also performed separately without ultrasonic irradiation and without catalyst as control group.

2.6. Active species trapping experiment for piezoelectric-catalytic degradation

Similar active species trapping experiments to photocatalysis was also carried out for determination of the active species playing effective roles in the ultrasonic induced piezoelectric degradation. In this part, EDTA and IPA still function as the hole (h⁺) scavenger and hydroxyl radical (·OH) scavenger, respectively, and p-benzoquinone served as the superoxide radical scavenger.

2.7. ·O₂[−] and ·OH quantification experiments for piezoelectric-catalytic degradation

In order to determine the amount of ·O₂[−] generated from the photocatalytic system accurately, 0.0166 mM nitroblue tetrazolium (NBT) which can react with ·O₂[−] was utilized. The production of ·O₂[−] was quantitatively analyzed through recording the concentration of NBT with an UV-vis spectrophotometer based on the absorbance at 259 nm [25]. And inspired by the former work [26], terephthalic acid (TA), as a probe molecule for detecting photocatalytically generated ·OH radicals, was used to realize the detection and quantification of such radicals in the context of ultrasonic induced piezoelectric materials for the first time. Terephthalic acid forms the highly fluorescent 2-hydroxyterephthalic acid with a specific fluorescence emission maximum at wavelength of 455 nm when reacting with ·OH radicals. It works as a qualitative specific test method for ·OH radicals by measuring the fluorescence intensity (F97XP, China) at 425 nm with the excitation wavelength of 315 nm since the highly-corresponding linear relation between fluorescence intensity and concentration. The process of NBT transformation and TA-PL methods were also similar to the ultrasonically-induced piezoelectric-catalytic degradation, but with NBT and TA replacing the methyl orange.

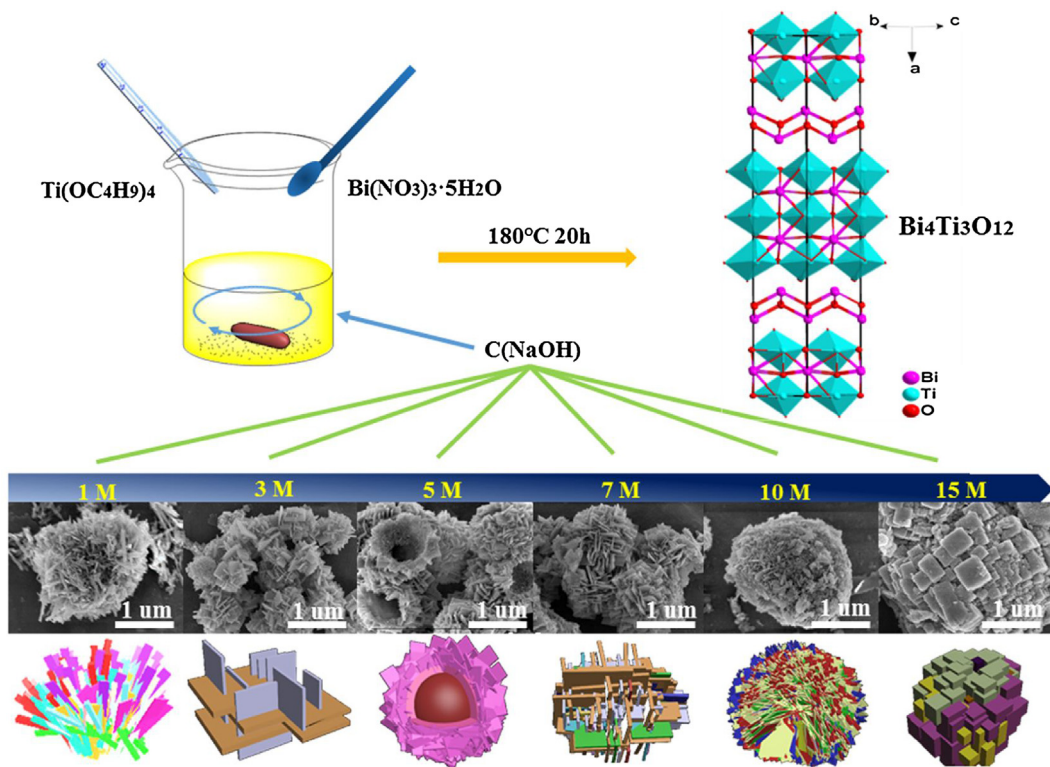
3. Results and discussion

3.1. Morphology control and structure characterizations

Presented in Fig. 1a are the XRD patterns of hydrothermally-synthesized Bi₄Ti₃O₁₂ with different NaOH concentrations. Broad

diffraction peaks with low intensity are observed for the samples synthesized at the NaOH concentrations of 1 M and 10 M, which means low crystallinity of samples under these conditions. It is seen that Bi₄Ti₃O₁₂ products obtained at 3–7 M NaOH show sharp and strong peaks, and their XRD patterns correspond well to the orthorhombic Bi₄Ti₃O₁₂ (JCPDS #35-0795). No impurity diffraction peaks were observed, demonstrating formation of pure-phase Bi₄Ti₃O₁₂. When the NaOH concentration raises to 10 M, Na_{0.5}Bi_{0.5}TiO₃ comes into being (JCPDS #46-0001), and the samples at 15 M NaOH is mainly composed of Na_{0.5}Bi_{0.5}TiO₃. It is concluded that the crystallinity of Bi₄Ti₃O₁₂ can be tuned by adjusting the mineralizer NaOH concentration. Fig. 1b displays the XRD pattern comparison between hydrothermally-synthesized Bi₄Ti₃O₁₂ (3 M) and Bi₄Ti₃O₁₂ obtained by sol-gel synthesis (SG-Bi₄Ti₃O₁₂). All the diffraction peaks of SG-Bi₄Ti₃O₁₂ are same to the hydrothermal Bi₄Ti₃O₁₂ in location but stronger in intensity, particularly the diffraction peak corresponding to {171} facet, uncovering a high degree of crystallinity in SG-Bi₄Ti₃O₁₂.

Scheme 1 shows the facile synthesis of Bi₄Ti₃O₁₂ with diverse morphologies by one-pot hydrothermal method. Without changing other reaction parameter but just adjusting the concentration of NaOH, diverse morphologies can be achieved. Bi₄Ti₃O₁₂ obtained at 1 M NaOH appears to be uniform nanorod-interlaced microstructure with same width of nearly 10 nm (Fig. 2a and b). Morphology and structure of the sample prepared in 3 M NaOH undergo great changes as it turns to be uniform microspheres with good dispersion (Fig. 2c), and these microspheres are composed of orthogonally-packed nanosheets with a square shape (Fig. 2d). The organizational form of Bi₄Ti₃O₁₂ synthesized in 5–7 M NaOH remains to be nanosheet-assembled, but more compactly, therefore turning the microsphere into larger size with a diameter of about 1 μm (Fig. 2e and g). It is worth noting that the microspheres reveal a nest-like hollow structure with its shell orderly packaging by similar sized nanosheets with the edge length of 200 nm and thickness of 20 nm (Fig. 2f and h). This hollow sphere and nanosheets structure tend to be replaced by other new forms as the broken nanosheets are gradually drowned out by particles with no fixed shape, and the independent spheres begin to reunite (Fig. 2i and j). When the concentration of NaOH increases to 15 M (Na_{0.5}Bi_{0.5}TiO₃), another regular shape that could be described as cube-assembled spheres formed and the individual sphere grows to much larger with diameter of 3–4 μm (Fig. 2k and m). Aggregating growth as well as the individual getting larger at higher concentration can be ascribed to the Oswald ripening process [27]. To sum



Scheme 1. Synthetic illustration for $\text{Bi}_4\text{Ti}_3\text{O}_{12}$ samples with diverse morphologies.

up the results above, morphology-controllable $\text{Bi}_4\text{Ti}_3\text{O}_{12}$ were easily realized by manipulating the mineralizer NaOH concentration in the one-pot hydrothermal process. Based on related references, we try to explain how the concentration of NaOH changes the morphology of the final $\text{Bi}_4\text{Ti}_3\text{O}_{12}$ products. It is reported that the increase of OH^- concentration can enhance the dissolved and crystallized process, especially affect the structural forms of growth units, and the growth interfaces. The Na^+ affects the crystal growth process mainly through adsorption on the surface. While $\text{Bi}_4\text{Ti}_3\text{O}_{12}$ crystal grows in 1 M NaOH , little Na^+ is adsorbed on the crystal surface of $\text{Bi}_4\text{Ti}_3\text{O}_{12}$ or has a small hindrance effect on the crystal growth, so a stronger crystalline orientation appears, leading to the nanowire-like structure. In 3 M NaOH , a larger amount of Na^+ ions are adsorbed on the $\{110\}$ plane of $\text{Bi}_4\text{Ti}_3\text{O}_{12}$ crystal, and the growth rate along a axis and c axis is much faster than that along b axis, resulting in $\text{Bi}_4\text{Ti}_3\text{O}_{12}$ plates which further assemble into microspheres. And in 5–7 M NaOH , a higher nucleation rate than the crystal growth rate causes the agglomeration of the crystal nuclei and leads to the formation of larger and compact microspheres. When the concentration of NaOH rises to 10 M or higher, convection of solute is disturbed and thus restrains the ordered growth of crystal, which explains the morphology of unordered assembly by incomplete plates.

As the morphology of products undergoes large change, specific surface area has been determined by N_2 adsorption-desorption method. The specific surface area of hydrothermally synthesized $\text{Bi}_4\text{Ti}_3\text{O}_{12}$ in different NaOH concentrations is $10.6 \text{ m}^2 \text{ g}^{-1}$ (1 M), $28.3 \text{ m}^2 \text{ g}^{-1}$ (3 M), $30.6 \text{ m}^2 \text{ g}^{-1}$ (5 M), $24.2 \text{ m}^2 \text{ g}^{-1}$ (7 M) and $14.3 \text{ m}^2 \text{ g}^{-1}$ (10 M), respectively.

EDX pattern of $\text{Bi}_4\text{Ti}_3\text{O}_{12}$ microspheres (Fig. S1) confirmed the existence of the three constituent elements: Bi, Ti, and O. The ratio of the three elements was estimated to be 17.33: 12.32: 50.36, further indicating the successful synthesis of pure $\text{Bi}_4\text{Ti}_3\text{O}_{12}$. Besides, EDX mapping (Fig. S1b–d) displayed the uniform distribution of Bi, Ti, and O elements in $\text{Bi}_4\text{Ti}_3\text{O}_{12}$ sample.

The morphology of $\text{Bi}_4\text{Ti}_3\text{O}_{12}$ obtained by sol-gel synthesis (SG- $\text{Bi}_4\text{Ti}_3\text{O}_{12}$) is also investigated and compared. SG- $\text{Bi}_4\text{Ti}_3\text{O}_{12}$ shows a great dissimilitude in morphology features with a tight aggregation formed by chunk slabs with length of 0.5–1 μm , which is much larger than that of the $\text{Bi}_4\text{Ti}_3\text{O}_{12}$ nanosheets (Fig. 3a and b). Such visual result was also reflected by the specific surface area comparison (Fig. 3c) that the surface area of hydrothermal $\text{Bi}_4\text{Ti}_3\text{O}_{12}$ ($28.3 \text{ m}^2 \text{ g}^{-1}$) was nearly 17 times bigger than the SG- $\text{Bi}_4\text{Ti}_3\text{O}_{12}$ ($1.6 \text{ m}^2 \text{ g}^{-1}$). N_2 adsorption-desorption isotherms of the hydrothermal $\text{Bi}_4\text{Ti}_3\text{O}_{12}$ microsphere was given in Fig. 3d. The adsorption–desorption isotherms with a occlusive hysteresis loop exhibit a downward bulge during the entire pressure range without inflection, yet no platform appears when the relative pressure reaches close to the saturated vapor pressure. The presented typical H3 class hysteresis loop corresponds well with the morphology feature of loosely-assembled nanosheets with wedge space as revealed from SEM images.

For further accurate morphology analysis and what's more, the crystal facet judgement, TEM was employed to analyze the as-synthesized $\text{Bi}_4\text{Ti}_3\text{O}_{12}$ (3 M NaOH). It confirms the assembled microstructure by orthogonally-packed square nanosheets (Fig. 4a and b). HRTEM image captured from a typical individual nanosheet reveals clear lattice fringes with the measured interplanar spacing of approximately 0.381 nm (Fig. 4c) which corresponds to the $\{111\}$ plane. The inset SAED image confirms that the $\text{Bi}_4\text{Ti}_3\text{O}_{12}$ nanosheet is a single crystal and well matches the above message, and the exposed facet of the nanosheet can be concluded to be $\{01-1\}$ facet, as demonstrated in Fig. 4d.

3.2. Photoabsorption and band gap

Optical properties of hydrothermally and so-gel synthesized $\text{Bi}_4\text{Ti}_3\text{O}_{12}$ samples were investigated using UV-vis diffuse reflection spectra. It is obvious that the absorption edge of hydrothermal $\text{Bi}_4\text{Ti}_3\text{O}_{12}$ (3–10 M NaOH) are all located at approximately 400 nm

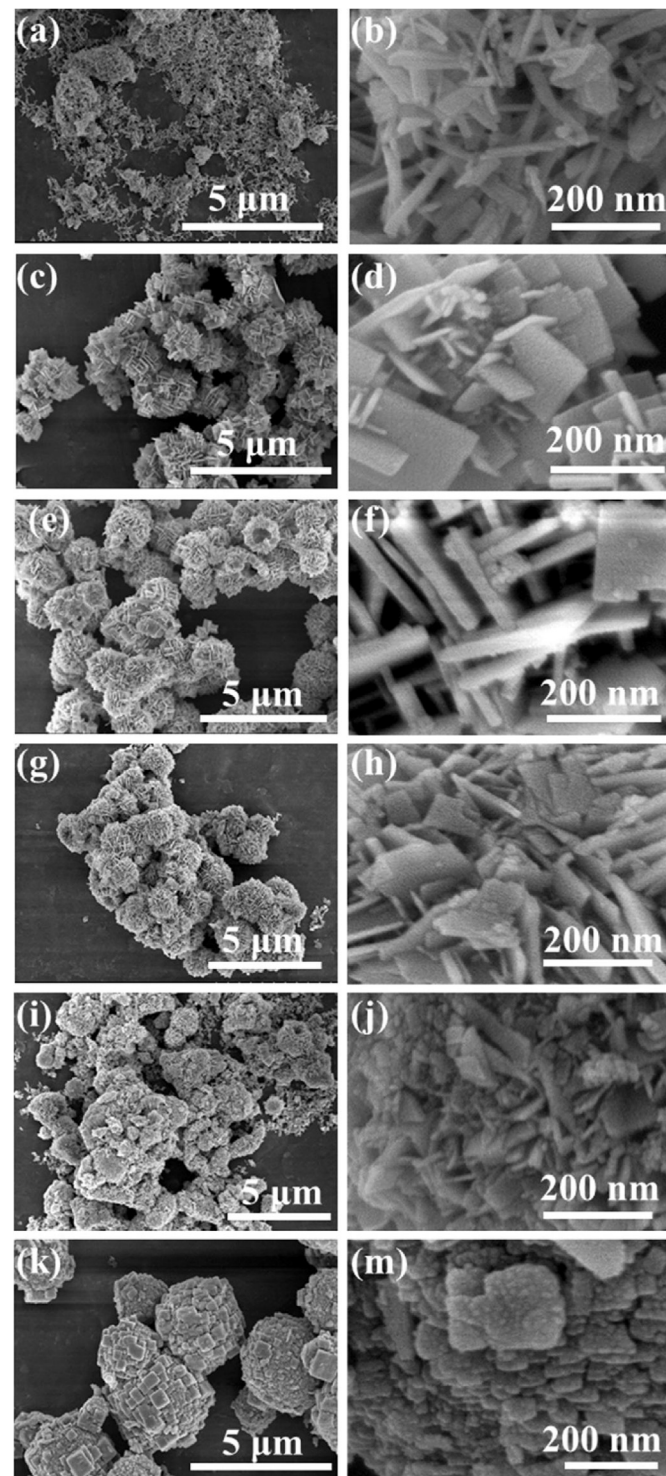


Fig. 2. SEM images of hydrothermally-synthesized $\text{Bi}_4\text{Ti}_3\text{O}_{12}$ with NaOH concentrations of (a, b) 1 M, (c, d) 3 M, (e, f) 5 M, (g, h) 7 M, (i, j) 10 M and (k, m) 15 M.

(Fig. 5a). There were no enormous difference in their light absorption and photo-responsive range, indicating the slight impact of various morphologies on photoabsorption. Compared with hydrothermal $\text{Bi}_4\text{Ti}_3\text{O}_{12}$ (3 M NaOH), SG- $\text{Bi}_4\text{Ti}_3\text{O}_{12}$ shows an extended absorption edge at 420 nm (Fig. 5b). The higher photoabsorption of hydrothermal $\text{Bi}_4\text{Ti}_3\text{O}_{12}$ below 370 nm than SG- $\text{Bi}_4\text{Ti}_3\text{O}_{12}$ should be attributed to the multiple reflection and scattering from the spherical structure.

Band gap values of samples were calculated using the following equation [28]:

$$h\nu = A(h\nu - Eg)^{n/2} \quad (1)$$

A is the absorption coefficient near the absorption edge; h represents the Planck's constant (eV); Eg is the absorption band gap energy; and $n=4$ for $\text{Bi}_4\text{Ti}_3\text{O}_{12}$ [10]. Thus the band gaps here were estimated to be 3.20 eV and 3.29 eV for the SG- $\text{Bi}_4\text{Ti}_3\text{O}_{12}$ and hydrothermal $\text{Bi}_4\text{Ti}_3\text{O}_{12}$, respectively.

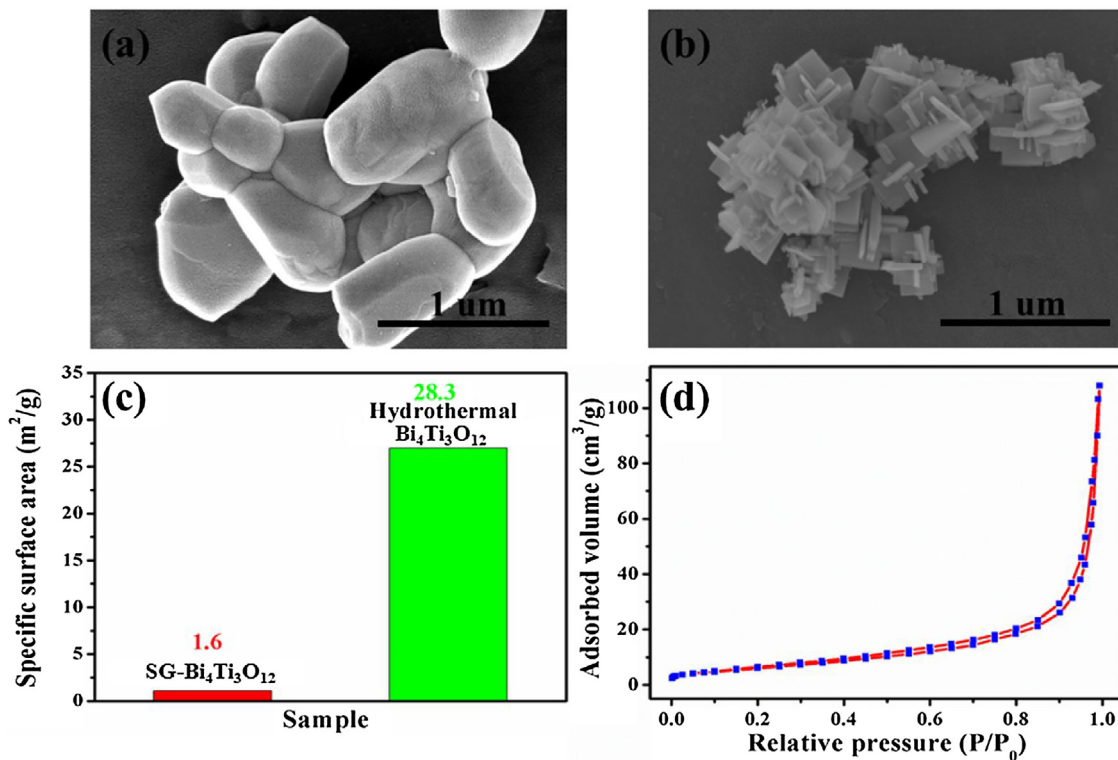


Fig. 3. SEM images of (a) SG- $\text{Bi}_4\text{Ti}_3\text{O}_{12}$ and (b) hydrothermal $\text{Bi}_4\text{Ti}_3\text{O}_{12}$ (3 M). (c) The specific surface area comparison and (d) N_2 adsorption–desorption isotherms of hydrothermal $\text{Bi}_4\text{Ti}_3\text{O}_{12}$ (3 M).

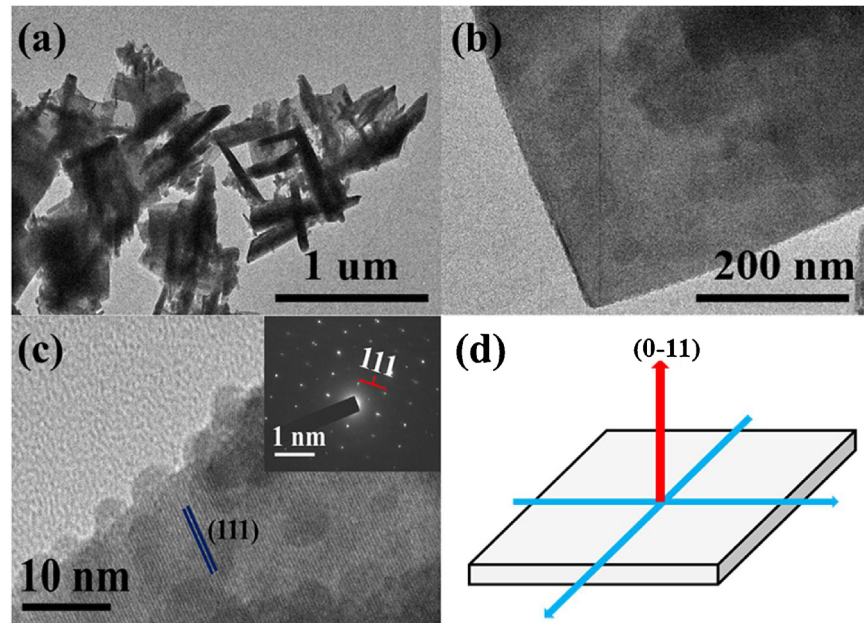


Fig. 4. (a, b) TEM image and (c) HRTEM image with the inset SAED pattern and (d) schematic diagram of the corresponding exposure facet of the hydrothermal $\text{Bi}_4\text{Ti}_3\text{O}_{12}$ (3 M).

3.3. Photocatalytic performance

3.3.1. Morphology-dependent photocatalysis for degradation of phenol

Photocatalytic activity of $\text{Bi}_4\text{Ti}_3\text{O}_{12}$ synthesized in different NaOH concentrations was assessed according to photo-degrading phenol exposing to ultraviolet light. The photodegradation efficiency of phenol as a function of irradiation time over

hydrothermally-synthesized samples was shown in Fig. 6a, where C_0 is the initial concentration of phenol, and C represents the concentration of remaining phenol at different times. The blank experiment (without catalyst) exhibits that irradiation alone was incapable of degrading phenol. Adsorption of the $\text{Bi}_4\text{Ti}_3\text{O}_{12}$ sample accounts for 15–25% of the removal of phenol due to the high specific surface area and unique structure. As for the photodegradation, one could see that $\text{Bi}_4\text{Ti}_3\text{O}_{12}$ with slice-assembled microsphere and

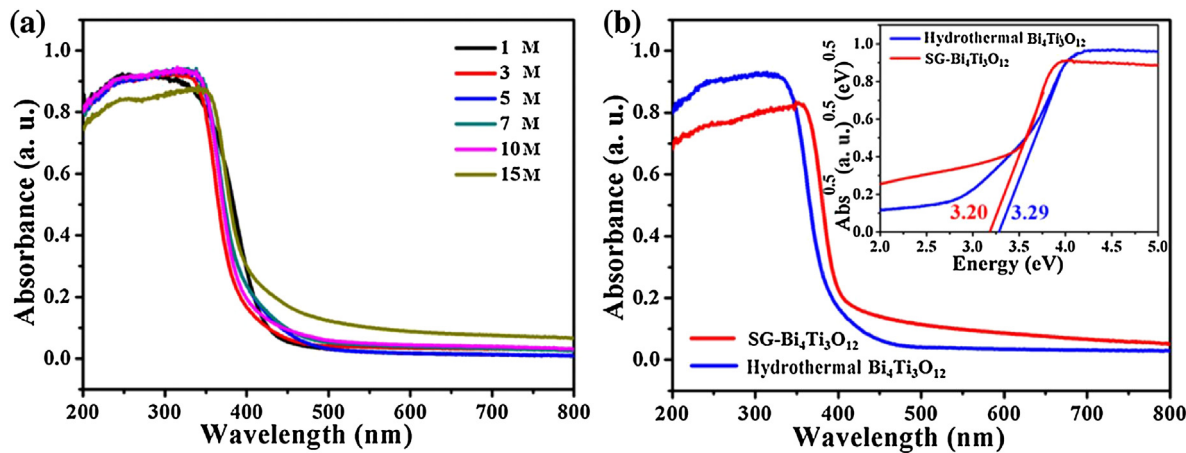


Fig. 5. (a) UV-vis absorption spectra of the $\text{Bi}_4\text{Ti}_3\text{O}_{12}$ samples synthesized in different NaOH concentration; (b) UV-vis absorption spectra and band gap (inset) of hydrothermal $\text{Bi}_4\text{Ti}_3\text{O}_{12}$ (3 M) and SG- $\text{Bi}_4\text{Ti}_3\text{O}_{12}$.

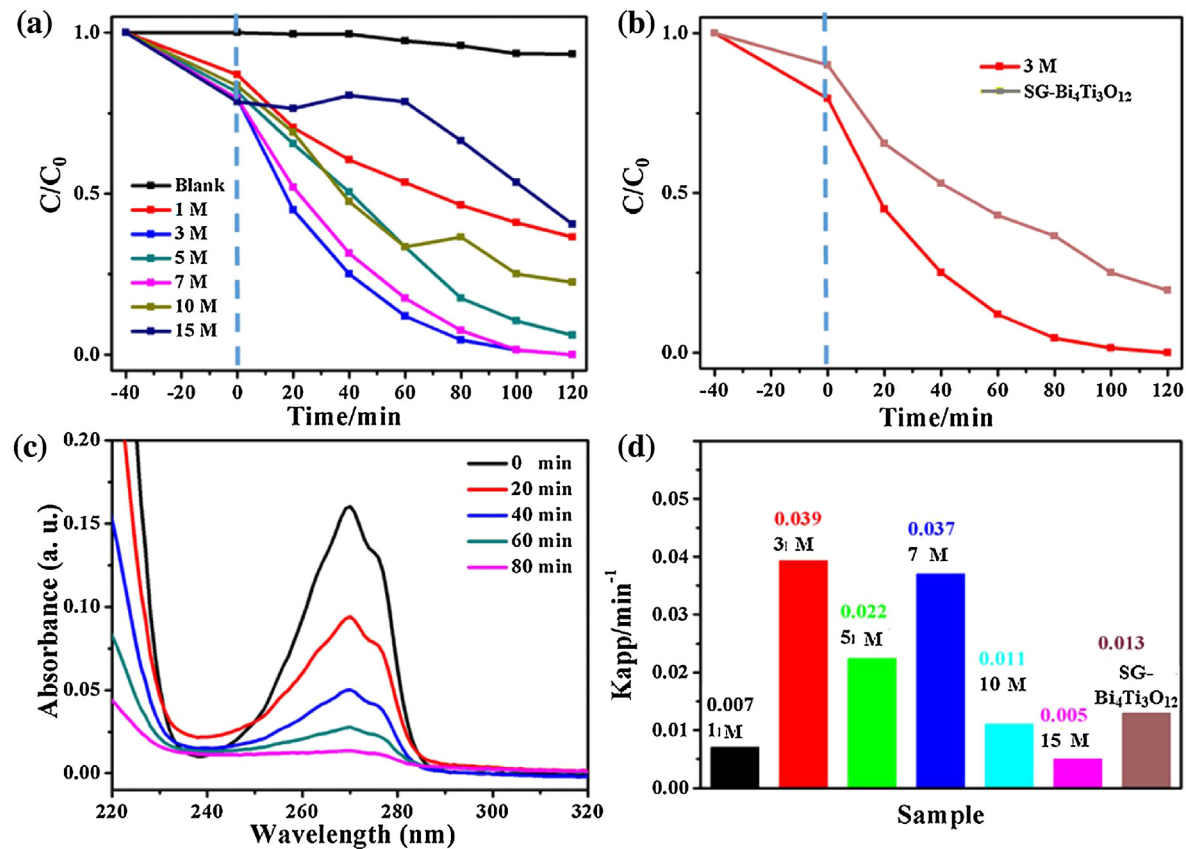


Fig. 6. Photocatalytic degradation curves of phenol over the hydrothermal (a) $\text{Bi}_4\text{Ti}_3\text{O}_{12}$ and (b) SG- $\text{Bi}_4\text{Ti}_3\text{O}_{12}$; (c) Temporal absorption spectra of phenol over hydrothermal $\text{Bi}_4\text{Ti}_3\text{O}_{12}$ (3 M); (d) Apparent rate constants for degrading phenol over all $\text{Bi}_4\text{Ti}_3\text{O}_{12}$ samples.

the hollow sphere structures (3–7 M NaOH) present greater photocatalytic activity than other samples, and $\text{Na}_{0.5}\text{Bi}_{0.5}\text{Ti}_3\text{O}_9$ (15 M NaOH) shows the lowest photoactivity. The 3 M $\text{Bi}_4\text{Ti}_3\text{O}_{12}$ microspheres exhibits the most excellent photocatalytic activity, which can remove 95% of phenol within 100 min irradiation. The higher performance of $\text{Bi}_4\text{Ti}_3\text{O}_{12}$ obtained with 3–7 M NaOH may probably be related to their high crystallinity, enabling a faster photogenerated electron transportation rate [29]. Photoluminescence spectra (Fig. 7) can reflect the recombination rate between holes and electrons among $\text{Bi}_4\text{Ti}_3\text{O}_{12}$ samples synthesized in different NaOH

concentrations. The recombination rate of catalysts with high crystallinity (3, 5, 7, 10 M) is lower than that of the samples with poor crystallinity (1 M), and 3 M $\text{Bi}_4\text{Ti}_3\text{O}_{12}$ displays the highest charge separation efficiency. These observations well correspond to the photodegradation result.

Besides, the adsorption and photocatalytic performance of the hydrothermal $\text{Bi}_4\text{Ti}_3\text{O}_{12}$ (3 M NaOH) is also much better than the SG- $\text{Bi}_4\text{Ti}_3\text{O}_{12}$, which should be attributed to the larger specific surface area of hydrothermal $\text{Bi}_4\text{Ti}_3\text{O}_{12}$ (Fig. 6b). Fig. 6c shows that the absorption band of phenol gradually decreases with irradiation

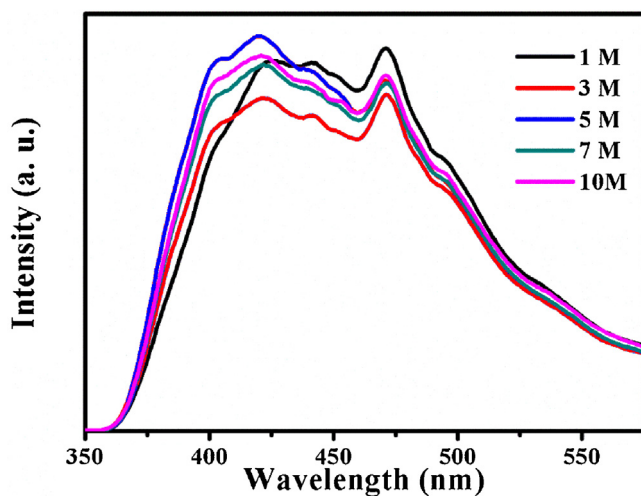


Fig. 7. Photoluminescence (PL) spectra of hydrothermal $\text{Bi}_4\text{Ti}_3\text{O}_{12}$ nanosheets excited at the light wavelength of 315 nm.

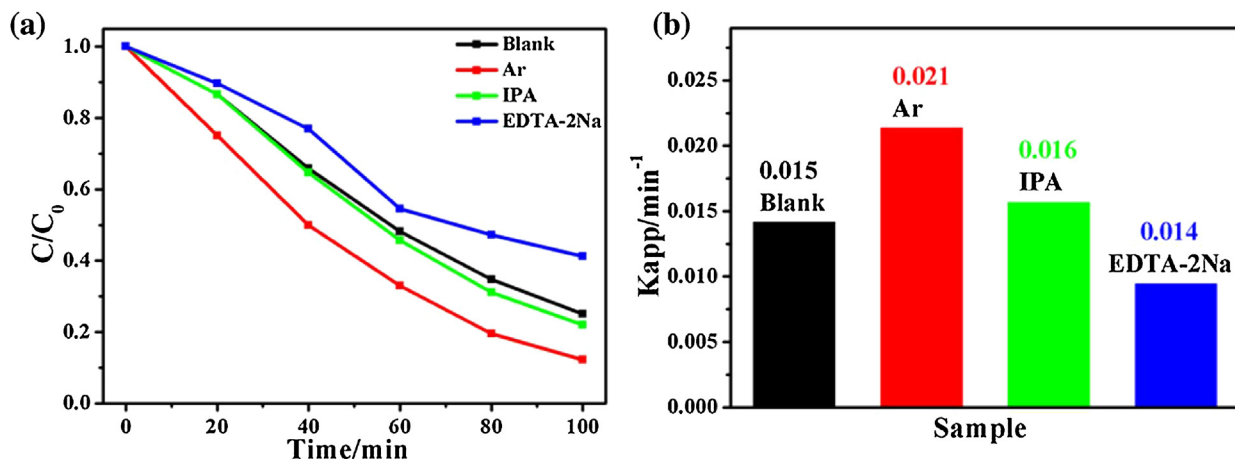


Fig. 8. (a) Photodegradation curves and (b) the related photodegradation rate constants of phenol over hydrothermal $\text{Bi}_4\text{Ti}_3\text{O}_{12}$ (3 M) alone and with addition of scavengers.

time, which may suggest the mineralization of phenol into H_2O and CO_2 . Reaction kinetics of phenol-degradation were calculated according to the pseudo-first-order equation [30]:

$$\ln(C_0/C) = k_{app}t \quad (2)$$

(C_0 : phenol concentration after adsorption for 40 min, C : instantaneous phenol concentration, k_{app} : rate constant at time t). The fastest photodegradation rate was observed for 3 M $\text{Bi}_4\text{Ti}_3\text{O}_{12}$ with a photodegradation rate constant of 0.039 min^{-1} , which is about 3 times that of SG- $\text{Bi}_4\text{Ti}_3\text{O}_{12}$ (0.013 min^{-1}). And the photodegradation keeps on when a smaller amount of catalyst (0.4 g/L) was used (Fig. S2). The photodegradation efficiency with catalyst concentration of 0.4 g/L is about 71.4% of that with catalyst concentration of 1 g/L .

3.3.2. Detection for active species of photocatalytic degradation

Reactive species involved in the photodegradation process was evaluated in order to investigate the photocatalytic mechanism. Disodium ethylenediaminetetraacetate (EDTA-2Na) and isopropyl alcohol (IPA) were chosen as the scavengers of hole (h^+) and hydroxyl radical ($\cdot\text{OH}$), respectively. In view of the instability of *p*-benzoquinone in phenol solution, O_2 isolation by bubbling argon was performed to inspect the formation of superoxide radical

($\cdot\text{O}_2^-$). As revealed in Fig. 8a and b, the addition of EDTA-2Na decreased the phenol photodegradation efficiency greatly, indicating that h^+ is the dominant reactive species. The photodegradation rate almost remains undiminished by adding IPA and bubbling Ar, which eliminated the possibility of $\cdot\text{O}_2^-$ and $\cdot\text{OH}$ functioning as the main active species.

3.3.3. Photocatalytic degradation of diverse pollutants and antibiotics

The universality for photocatalytic activity of $\text{Bi}_4\text{Ti}_3\text{O}_{12}$ photocatalyst was examined by photodegrading diverse industrial pollutants and antibiotics with different molecular structures, including chlorotetracycline, bisphenol A, rhodamine B and tetracycline hydrochloride, under the simulated solar irradiation. As illustrated in Fig. 9a, all the pollutants and antibiotics can be decomposed as irradiation goes on. The removal efficiencies of chlorotetracycline, bisphenol A and rhodamine B achieve 73.6%, 45.3% and 62.1%, respectively, after 4 h illumination. For tetracycline hydrochloride, it is more liable to be removed, and its removal efficiency reaches 42.3% only in 40 min. These results unfold that $\text{Bi}_4\text{Ti}_3\text{O}_{12}$ can function as a potential photocatalyst with unselective and outstanding photocatalytic performance.

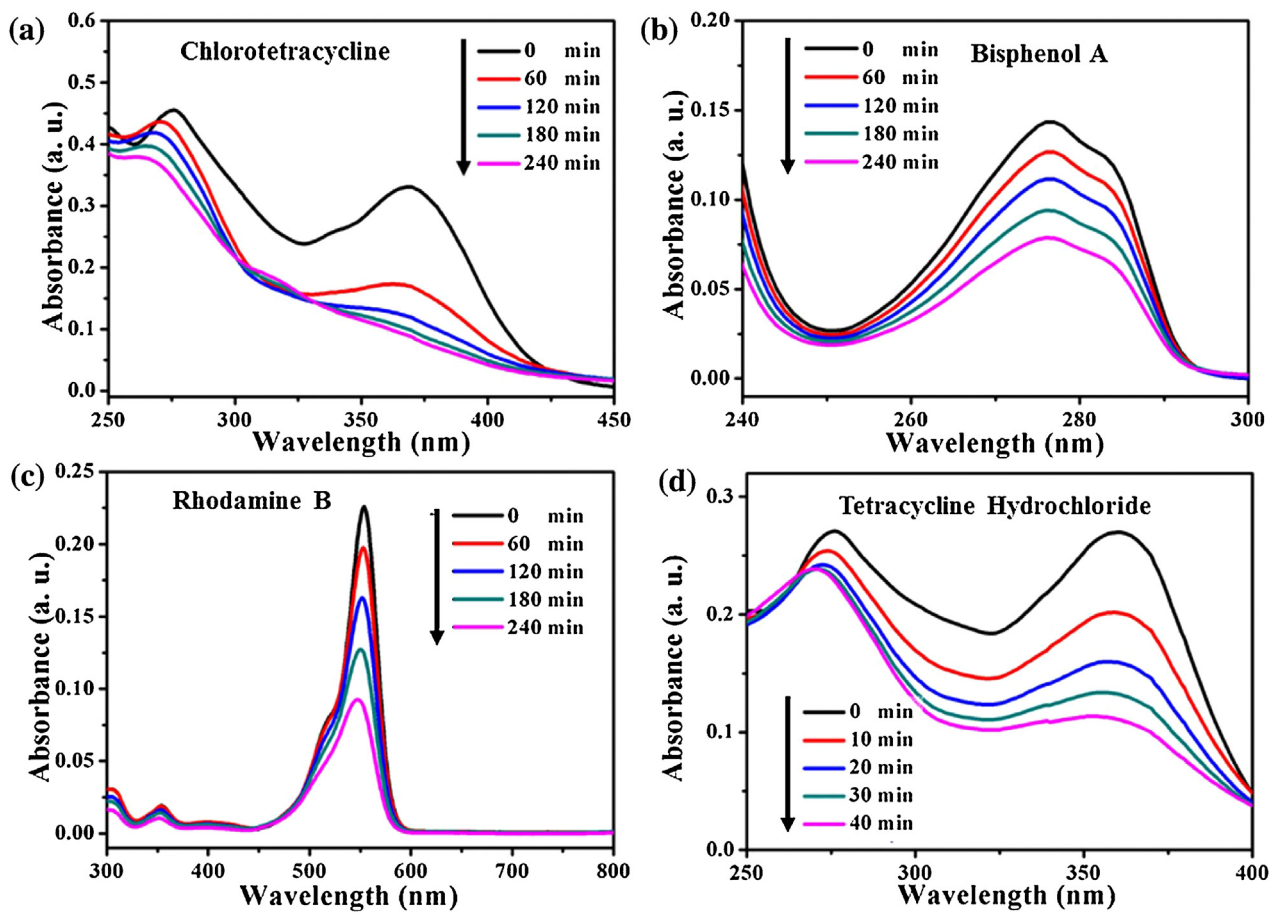


Fig. 9. Temporal absorption spectra of (a) chlorotetracycline, (b) bisphenol A, (c) rhodamine B, and (d) tetracycline hydrochloride over hydrothermal $\text{Bi}_4\text{Ti}_3\text{O}_{12}$ (3 M) under UV-vis light.

3.4. Ultrasonic-assisted piezoelectric-catalytic performance

3.4.1. Ultrasonic-assisted piezoelectric-catalysis for multiple contaminants degradation

The multiferro/piezoelectric behaviors of $\text{Bi}_4\text{Ti}_3\text{O}_{12}$ trigger us to investigate the piezoelectric-catalytic performance. Here, 3 M $\text{Bi}_4\text{Ti}_3\text{O}_{12}$ slice-assembled microspheres are employed as the catalyst, and dye model methyl orange (MO) was selected as the degradation target. Ultrasonic cleaner (40 kHz, 300 W) equipped with an electric stirrer provides press to drive the piezoelectric-catalytic reaction. The scheme for equipment and piezoelectric-catalytic reaction is shown in Fig. 10a. The MO concentration in the absence of $\text{Bi}_4\text{Ti}_3\text{O}_{12}$ remains unchanged with 6 h continuous ultrasonic irradiation, which eliminates the possibility that ultrasonic can directly degrade MO (Fig. 10b). A slight decrease in MO concentration for $\text{Bi}_4\text{Ti}_3\text{O}_{12}$ without ultrasonic should be related to the adsorption of $\text{Bi}_4\text{Ti}_3\text{O}_{12}$. Notably, large decrease in the MO concentration was observed for $\text{Bi}_4\text{Ti}_3\text{O}_{12}$ subjected to external ultrasonic vibration, which achieves a decomposition efficiency of more than 80% MO within 6 h ultrasonic irradiation (Fig. 10c). What's more, no new absorption band emerging at any other wavelength along with the MO absorbance at 463 nm gradually disappearing tells the achievement to some level of MO mineralization into H_2O and CO_2 [31]. Though the above ultrasonic-assisted degradation experiments were conducted below 45 °C with frequent water inflow-outflow operation, to further rule out the local heating effect induced by ultrasonic, the piezoelectric catalytic degradation of MO in ice-water bath were also performed where the temperature was kept at 0 °C all the time. As shown in Fig. 10b, no obvious

change occurred for the degradation curve in ice-water bath compared with at room temperature (below 45 °C). It indicates that the effect of local heating during the ultrasonic process on degradation can be excluded, further confirming the piezoelectric catalytic degradation. In addition, piezoelectric-catalytic degradation performance of SG- $\text{Bi}_4\text{Ti}_3\text{O}_{12}$ was also investigated, the result shows the hydrothermal $\text{Bi}_4\text{Ti}_3\text{O}_{12}$ and SG- $\text{Bi}_4\text{Ti}_3\text{O}_{12}$ present little difference in piezoelectric-catalytic MO degradation (Fig. S3). Thus, we can conclude that difference in the morphology and specific surface area between hydrothermal $\text{Bi}_4\text{Ti}_3\text{O}_{12}$ and SG- $\text{Bi}_4\text{Ti}_3\text{O}_{12}$ may exert slight impact on the piezoelectric-catalytic degradation performance of $\text{Bi}_4\text{Ti}_3\text{O}_{12}$. Moreover, the piezoelectric-catalytic degradation efficiency almost remains unchanged when the amount of catalyst was cut in half (Fig. S4), demonstrating that the piezoelectric-catalytic degradation is less dependent on catalyst concentration than photodegradation.

To inspect the universality for piezoelectric-catalytic activity of $\text{Bi}_4\text{Ti}_3\text{O}_{12}$, the piezoelectric-catalytic degradation of bisphenol A and tetracycline hydrochloride as representatives of phenols and antibiotics were selected as the target contaminants. As illustrated in Fig. 10d and e, both bisphenol A and tetracycline hydrochloride can be degraded by piezoelectric-catalysis. The removal efficiency of bisphenol A achieves 65.6% after 4 h ultrasonic treatment. A higher removal efficiency for tetracycline hydrochloride was obtained, which reaches 81.4% only within 40 min. These results disclose that $\text{Bi}_4\text{Ti}_3\text{O}_{12}$ shows unselective piezoelectric-catalytic activity for treating contaminants and antibiotics.

Moreover, the piezoelectric-catalytic degradation of MO with different ultrasonic powers (300 W, 225 W and 150 W) is also per-

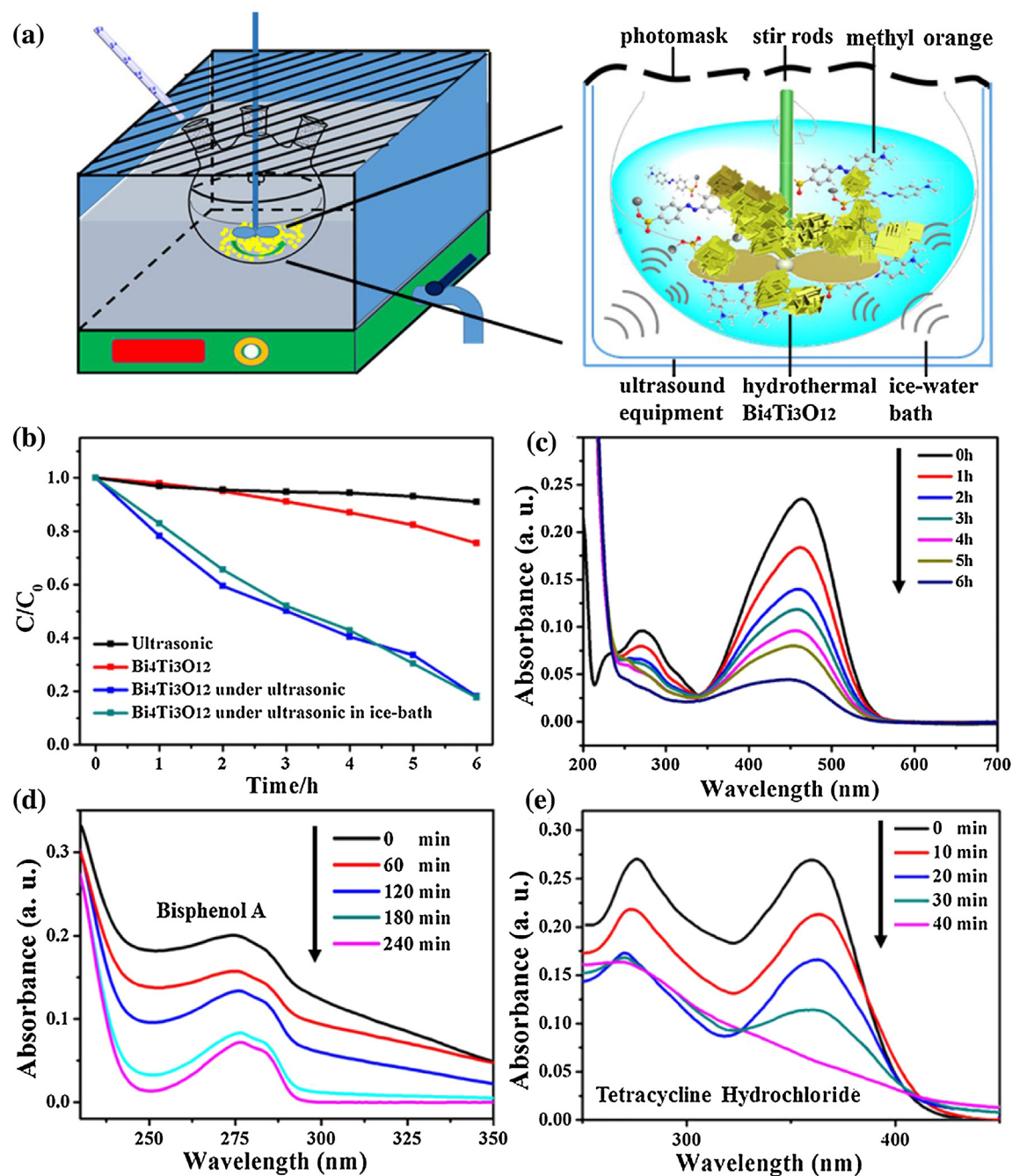


Fig. 10. (a) Schematic illustration for ultrasonic-assisted piezoelectric-catalytic degradation of MO; (b) Piezoelectric-catalytic degradation curves of methyl orange solution over $\text{Bi}_4\text{Ti}_3\text{O}_{12}$, ultrasonic (40 kHz, 300 W) and $\text{Bi}_4\text{Ti}_3\text{O}_{12}$ with irradiation of ultrasonic (40 kHz, 300 W); (c) The corresponding absorption spectra of MO with ultrasonic time; Absorption spectra of bisphenol A (d) and tetracycline hydrochloride (e) with ultrasonic time (40 kHz, 300 W).

formed. As shown in Fig. 11a and b, the degradation efficiency descends with the decrease of ultrasonic power, which is in positive correlation with ultrasonic power. It confirms the occurrence of piezoelectric-induced catalysis.

3.4.2. Radicals quantification and piezoelectric-catalytic degradation mechanism exploration

To probe the piezoelectric-catalytic degradation mechanism, active species capture experiment used in photodegradation was introduced to realize the qualitative analysis of active species that take part in the ultrasonic-induced degradation. Compared with blank group, the degradation efficiency with adding EDTA-2Na suffers no influence during the ultrasonic irradiation period (Fig. 12a),

excluding h^+ as active species. Interestingly, there's almost no degradation of methyl orange observed through adding BQ and less degradation in the group with addition of IPA, revealing that $\bullet\text{O}_2^-$ is the main active species responsible for the efficient MO degradation and $\bullet\text{OH}$ plays the second fiddle.

For further confirmation and provide in-depth insight into understanding the active radicals, $\bullet\text{O}_2^-$ and $\bullet\text{OH}$ are quantitatively determined. Nitroblue tetrazolium (NBT) was chosen to quantify the $\bullet\text{O}_2^-$ concentration produced by $\text{Bi}_4\text{Ti}_3\text{O}_{12}$ (Fig. 12c). The absorbance of NBT molecule at 259 nm shows a trend of gradual and great decrease with prolonging the ultrasonic time, which indicates the continuous production for large amount of $\bullet\text{O}_2^-$. According to the reaction equation that 1 mol NBT could react with

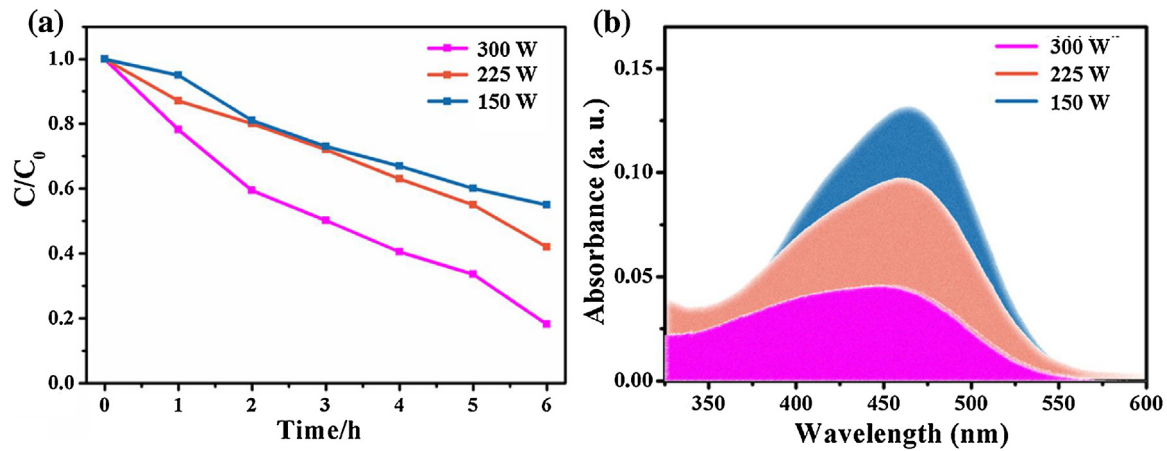
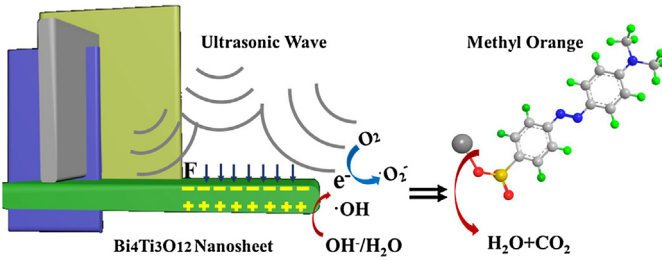


Fig. 11. Piezoelectric-catalytic degradation curves of MO (a) and absorption spectra of MO after 6 h ultrasonic irradiation (b) using different ultrasonic powers.

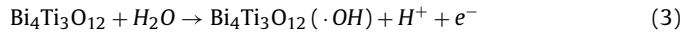


Scheme 2. Schematic illustration for ultrasonic-induced piezoelectric-catalysis of $\text{Bi}_4\text{Ti}_3\text{O}_{12}$ for degrading methyl orange.

4 mol $\cdot\text{O}_2^-$ [32], the concentration of $\cdot\text{O}_2^-$ produced with ultrasonic irradiation time can be determined, as shown in Fig. 12e. The average $\cdot\text{O}_2^-$ production rate was calculated to be $6.4 \mu\text{mol g}^{-1} \text{h}^{-1}$ (Fig. 12f). Terephthalic acid (TA) can react with $\cdot\text{OH}$ in equal proportion to engender the highly fluorescent 2-hydroxyterephthalic acid with emission peak at 425 nm. Thus, the concentration of $\cdot\text{OH}$ can be obtained by recording the PL emission intensity. As revealed in Fig. 10d, $\text{Bi}_4\text{Ti}_3\text{O}_{12}$ generates strong PL peak at 425 nm with excitation wavelength of 315 nm, and the PL peak intensity orderly strengthens with the continuous ultrasonic irradiation. It demonstrates generation of 2,5-dihydroxyterephthalic acid (TAOH) in a hydroxylation of terephthalic acid, thus vividly reflecting the production of $\cdot\text{OH}$ (Fig. 12d). According to the linear relation formula between concentration and PL intensity of TA (Fig. S5), the generation rate of $\cdot\text{OH}$ concentration was determined to be $2.4 \mu\text{mol g}^{-1} \text{h}^{-1}$ (Fig. 12e and f). Besides, two blank tests without addition of catalysts were conducted. Both of NBT and TA remain stable and show no changes under ultrasonic irradiation (Fig. S6). It indicates that only ultrasonic irradiation in the absence of catalyst has no impact on the interaction between NBT and $\cdot\text{O}_2^-$, and TA and $\cdot\text{OH}$.

Based on the above results from active species capture test, we attempt to conjecture the piezoelectric-catalytic degradation mechanism Scheme 2. It is reported that the ultrasonic can drive the materials to induce a piezoelectric semiconducting coupling process which could convert mechanical energy into electricity [33]. As a well-recognized piezoelectric material, the piezoelectricity of $\text{Bi}_4\text{Ti}_3\text{O}_{12}$ arises from the lack of inversion symmetry in its crystal structure, thereby resulting in distribution of positive and negative charges to the opposite sides, when $\text{Bi}_4\text{Ti}_3\text{O}_{12}$ suffers from external stress force along a certain direction. Here, the ultrasonic-introduced press would induce the generation of positive and negative charges on two opposite surfaces of $\text{Bi}_4\text{Ti}_3\text{O}_{12}$. The as-generated electric charges thus trigger the degradation reaction

via the electrocatalytic effect, and the reaction equation was further brought forward with the help of metal oxide adsorbed free radical theory [34]:



In this electro-catalytic process, $\text{Bi}_4\text{Ti}_3\text{O}_{12}$ could convert H_2O or OH^- into $\cdot\text{OH}$, which absorbs on the surface of $\text{Bi}_4\text{Ti}_3\text{O}_{12}$. At the same time, the electrons are generated, and then reduce O_2 into $\cdot\text{O}_2^-$. Under the attack of the two powerful radicals $\cdot\text{O}_2^-$ and $\cdot\text{OH}$, $\text{Bi}_4\text{Ti}_3\text{O}_{12}$ presents excellent degradation performance for MO, bisphenol A and tetracycline hydrochloride. When turning down the ultrasonic power, it causes a reduced force pressed on the nanosheet, and thus slows down the space charge conduction according to the proportional relation between force and electric density of fixed facet, resulting in a weak electrocatalytic effect of interface and finally affects the degradation rate. This proposed pathway may help to cognize and understand the piezoelectric-catalytic mechanism.

4. Conclusion

In summary, morphology controllable $\text{Bi}_4\text{Ti}_3\text{O}_{12}$, including nanorods, slice-assembled microspheres, nest-like hollow microspheres, and cube assembly ($\text{Na}_{0.5}\text{Bi}_{0.5}\text{TiO}_3$), were obtained by controlling the concentration of NaOH mineralizer in a facile one-pot hydrothermal process. The photocatalytic experiments for degradation of phenol demonstrate that the hydrothermally-derived $\text{Bi}_4\text{Ti}_3\text{O}_{12}$ microsphere shows the most excellent photodegradation activity, which also exceeds $\text{Bi}_4\text{Ti}_3\text{O}_{12}$ obtained by sol-gel route. It also presents universal photoreactivity for removing multiform contaminants and antibiotics, like bisphenol A, rhodamine B, chlorotetracycline and tetracycline hydrochloride, boding for its promising practical applications. Photogenerated holes are demonstrated to be the active species in the photocatalytic process. For the first time, the piezoelectric-catalytic performance of $\text{Bi}_4\text{Ti}_3\text{O}_{12}$ for degradation of methyl orange, bisphenol A and tetracycline hydrochloride under ultrasonic irradiation is reported. $\text{Bi}_4\text{Ti}_3\text{O}_{12}$ produces abundant powerful superoxide ($\cdot\text{O}_2^-$) and hydroxyl ($\cdot\text{OH}$) radicals with production rates of 6.4 and $2.4 \mu\text{mol g}^{-1} \text{h}^{-1}$ in the piezoelectric-catalytic process, accounting for the efficient degradation. The piezoelectric-catalytic mechanism as well as formation of these radicals is tentatively proposed, which attributes to an electrocatalysis-related effect. These findings unquestionably uncover a new horizon of materials which shows both photocatalysis and piezoelectric-catalysis for environmental applications.

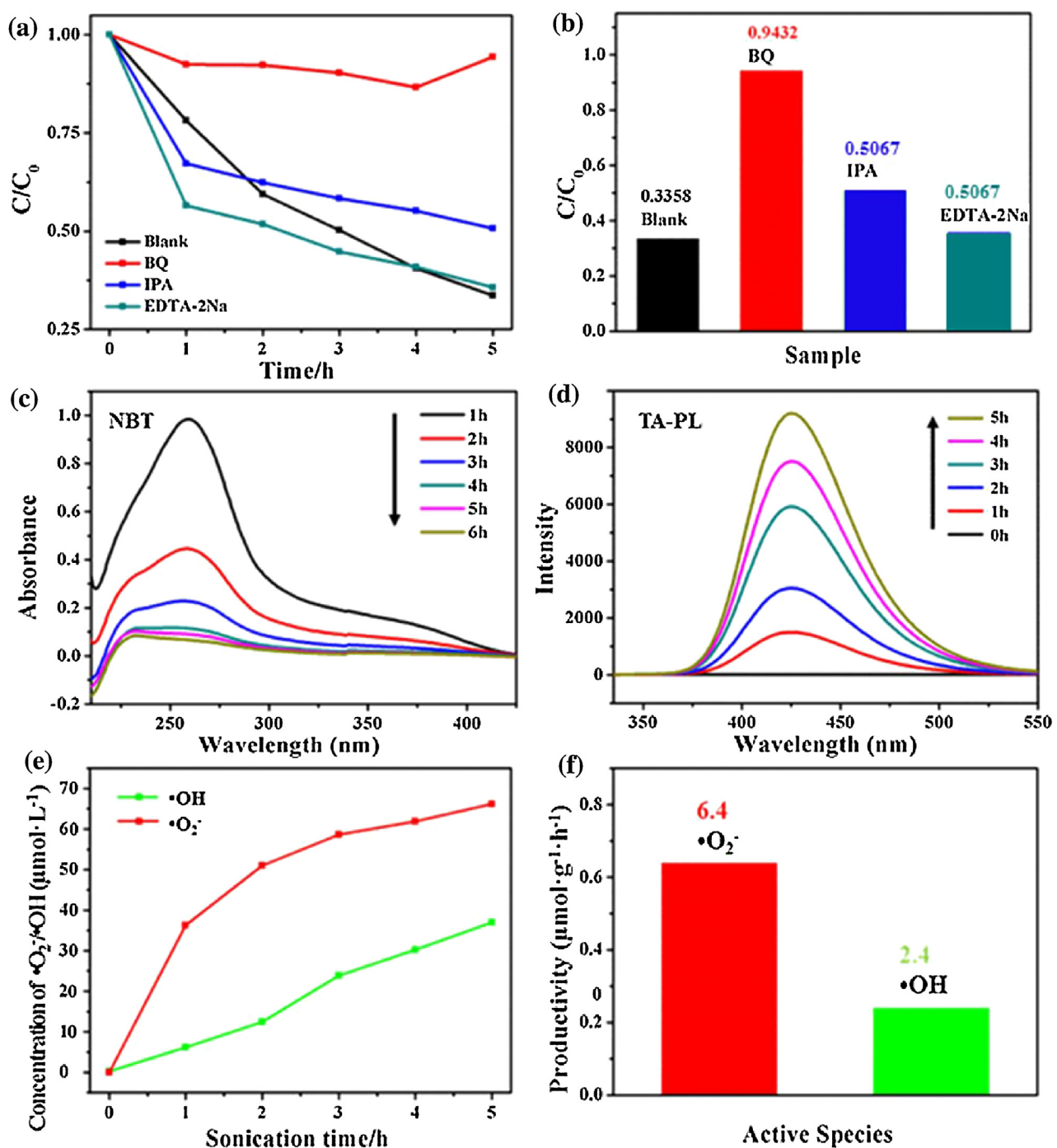


Fig. 12. (a) Piezoelectric-catalytic degradation curves and (b) efficiencies of MO with different scavengers; (c) Absorption spectra of NBT and (d) fluorescence spectra of TAOH solution over $\text{Bi}_4\text{Ti}_3\text{O}_{12}$ with 5 h ultrasonic irradiation; (e) Concentration curves of $\bullet\text{O}_2^-$ and (f) $\bullet\text{OH}$ vs. irradiation time produced by $\text{Bi}_4\text{Ti}_3\text{O}_{12}$ and (f) the corresponding productivity.

Competing interest

The authors declare no competing financial interest.

Acknowledgement

This work was jointly supported by the National Natural Science Foundations of China (Grant No. 51672258 and 51572246), the Fundamental Research Funds for the Central Universities (2652015296).

Appendix A. Supplementary data

Supplementary data associated with this article can be found, in the online version, at <http://dx.doi.org/10.1016/j.apcatb.2017.08.001>.

References

- [1] S. Bai, X.Y. Li, Q. Kong, R. Long, C.M. Wang, J. Jiang, Y.J. Xiong, *Adv. Mater.* 27 (2015) 3444–3452.
- [2] S.B. Wang, Y.H. Zhang, T.R. Zhang, F. Dong, H.W. Huang, *Appl. Catal. B-Environ.* 208 (2017) 75–81.

[3] H. Li, J. Shang, Z.H. Ai, L.Z. Zhang, *J. Am. Chem. Soc.* 137 (2015) 6393–6399.

[4] P. Zhang, X. Hua, X.X. Teng, D.S. Liu, Z.H. Qin, S.M. Ding, *Mater. Lett.* 185 (2016) 275–277.

[5] H.W. Huang, X.W. Li, J.J. Wang, F. Dong, P.K. Chu, T.R. Zhang, Y.H. Zhang, *ACS Catal.* 5 (2015) 4094–4103.

[6] H.W. Huang, Y. He, Z.S. Lin, L. Kang, Y.H. Zhang, *J. Phys. Chem. C* 117 (2013) 22986–22994.

[7] H.W. Huang, Y. He, X.W. Li, M. Li, C. Zeng, F. Dong, X. Du, T.R. Zhang, Y.H. Zhang, *J. Mater. Chem. A* 3 (2015) 24547–24556.

[8] J. Jiang, K. Zhao, X.Y. Xiao, L.Z. Zhang, *J. Am. Chem. Soc.* 10 (2012) 4473–4476.

[9] F. Wang, J.B. Wang, X.L. Zhong, B.L. Li, Y. Zhang, Y.C. Zhou, *Mater. Lett.* 121 (2014) 22–25.

[10] C.A.P. Dearaujo, J.D. Cuchiaro, L.D. McMillan, M.C. Scott, J.F. Scott, *Nature* 374 (1995) 627.

[11] Y.F. Cui, J. Briscoe, S. Dunn, *Chem. Mater.* 25 (2013) 4215–4223.

[12] Z.W. Chen, H. Jiang, W.L. Jin, C.K. Shi, *Appl. Catal. B–Environ.* 180 (2016) 698–706.

[13] Z.W. Chen, X.Y. Jiang, C.B. Zhu, C.K. Shi, *Appl. Catal. B–Environ.* 199 (2016) 241–251.

[14] F. Wang, J.B. Wang, X.L. Zhong, B.L. Li, Y. Zhang, Y.C. Zhou, *Mater. Lett.* 121 (2014) 22–25.

[15] F. Wang, J.B. Wang, X.L. Zhong, B. Li, J. Liu, D. Wu, D. Mo, D.Y. Guo, S.G. Yuan, K.D. Zhang, Y.C. Zhou, *CrystEngComm* 15 (2013) 1397–1403.

[16] X. Lin, P. Lv, Q.F. Guan, H.B. Li, H.J. Zhai, C.B. Liu, *Appl. Surf. Sci.* 258 (2012) 7146–7153.

[17] X.D. Wang, J.H. Song, J. Liu, Z.L. Wang, *Science* 316 (2007) 102–105.

[18] Z.L. Wang, J.H. Song, *Science* 312 (2006) 242–246.

[19] K.S. Hong, H.F. Xu, H. Konishi, X.C. Li, *The J. Phys. Chem. Lett.* 1 (2010) 997–1002.

[20] H. Lin, Z. Wu, Y.M. Jia, W.J. Li, R.K. Zheng, H.S. Luo, *Appl. Phys. Lett.* 104 (2014) 162907.

[21] G. Sudarjanto, B. Keller-Lehmann, J. Keller, J. Hazard. Mater. 138 (2006) 160–168.

[22] I.K. Konstantinou, T.A. Albanis, *Appl. Catal. B–Environ.* 49 (2004) 1–14.

[23] H.J. Zhang, G. Chen, X. Li, *Solid State Ion.* 180 (2009) 1599–1603.

[24] L.Q. Ye, J.Y. Liu, C.Q. Gong, L.H. Tian, T.Y. Peng, L. Zan, *ACS Catal.* 2 (2012) 1677–1683.

[25] L.Q. Ye, J.Y. Liu, Z. Jiang, T.Y. Peng, L. Zan, *Appl. Catal. B–Environ.* 142 (2013) 1–7.

[26] A. Benke, E. Mehner, M. Rosenkranz, E. Dmitrieva, T. Leisegang, H. Stoecker, W. Pompe, D.C. Meyer, *J. Phys. Chem.* 100 (2015) 18278–18286.

[27] R.D. Vengrenovich, Y.V. Gudyma, S.V. Yarema, *Semiconductors* 35 (2001) 1378–1382.

[28] D. Hou, W. Luo, Y. Huang, J.C. Yu, X. Hu, *Nanoscale* 5 (2013) 2028.

[29] Q.Q. Shen, J.B. Xue, H.C. Zhao, M.Z. Shao, X.G. Liu, H.S. Jia, *J. Alloy. Compd.* 695 (2016) 1080–1087.

[30] C.Y. Liu, H.W. Huang, X. Du, T.R. Zhang, N. Tian, Y.X. Guo, Y.H. Zhang, *J. Phys. Chem. C* 119 (2015) 17156–17165.

[31] S. Naraginti, F.B. Stephen, A. Radhakrishnan, A. Sivakumar, *Spectrochim. Acta A* 135 (2015) 814.

[32] L.Q. Ye, K.J. Deng, F. Xu, L.H. Tian, T.Y. Peng, L. Zan, *Phys. Chem. Chem. Phys.* 14 (2012) 82–85.

[33] N.C. Eddingsaas, K.S. Suslick, *Nature* 444 (2006) 163.

[34] C. Comninellis, *Electrochim. Acta* 39 (1994) 1857–1862.